Supplementary Materials for

The 2020 M_w 6.5 Monte Cristo Range, Nevada earthquake: relocated seismicity shows rupture of a complete shear-crack system

Anthony Lomax[1]

[1]ALomax Scientific, Mouans-Sartoux, France.

Corresponding author: Anthony Lomax (anthony@alomax.net)

The PDF file includes:

- Methods S1. Source-specific station term corrections
- Methods S2. Absolute, coherency relocation
- Methods S3. FMAMP – Probabilistic focal-mechanism determination
- Fig. S1. Velocity models used for location.
- Fig. S2. Map view of Monte Cristo seismicity with different location procedures.
- Fig. S3. Relocations of Monte Cristo mainshock and 5 foreshocks.

Other Supplementary Material for this manuscript includes the following:

- Data set S1 (CSV format). Seismicity catalog of NLL-SSST-coherence relocated events. http://alomax.free.fr/eartharxiv/MonteCristo_2020/v1/Supp_Files/DataSetS1_MonteCristo2020_NLL_SSST_coherence.csv
- Movie S1 (MP4 format). Fly-around animation of the NLL-SSST-coherence relocated seismicity in 3D. http://alomax.free.fr/eartharxiv/MonteCristo_2020/v1/Supp_Files/MovieS1_MonteCristo2020_ALomax_NLL-SSST-coherence_movie_60_20201015_small.mp4

Supplementary materials

Methods S1. Source-specific station term corrections

We perform a first stage of absolute earthquake locations to generate source-specific station term corrections (SSST, *1*) to improve the relative location and clustering of events. In contrast to station static corrections (*2–6*) which give a unique time correction for each station and phase type, SSST corrections vary smoothly within a 3D volume to specify a source-position dependent correction for each station and phase type. Spatial-varying, SSST corrections are most important when the ray paths between stations and different studied events differ, such as when stations are within the studied seismicity, the extent of seismicity is large relative to the distance to the stations, or the depth range of events is large. SSST corrections may increase in utility as errors in the velocity model increase, such as when a 1D or large-wavelength model is used in an area of small scale, 3D heterogeneity.

Within the NonLinLoc package (*7*, *8*), SSST corrections can be developed iteratively with a Gaussian spatial smoothing kernel of decreasing size. Given an initial set of event locations made without station corrections, 3D grids of SSST corrected travel-times for each station-phase are created iteratively by:

1 At each node in the corrected travel-time grid and for each station-phase:

1.a Accumulate the weighted mean of residuals, $\bar{R}$, for the station-phase for each event location exceeding specified quality criteria. The weights are given by,

$$w = \exp\left(-d^2/D^2\right) + \epsilon, \tag{S1}$$

where d is the distance between the grid node and the event hypocenter, D is the smoothing distance, and ϵ is a small value to give finite weight for all events and thus non-zero corrections even if and event hypocenters is far from the grid node.

1.b Add $\bar{R}$ as the current SSST correction to the previous travel-time for the station-phase at the node and store at the node in the updated SSST corrected travel-time grid.

2 Relocate all events using the updated SSST corrected travel-times.

3 Reduce D and return to step 1 if $D \geq$ the smallest required smoothing distance.

For the case of a grid node far from all event hypocenters, all weights will be approximately ϵ, and $\bar{R}$ will be close to the station static correction for the set of locations. Similarly, if the starting value of D is large relative to the extent of stations and hypocenters, then $\bar{R}$ for all station-phases will be close to the station static correction for the set of locations

For the Monte Cristo study, we iteratively generating SSST corrections using only events which have arrival data at one of the nearby temporary stations (NN.MC01, NN.MC02, NN.MC03 GS.MCA04, NN.MCA06, NN.MCM05, NN.MCM07, NN.MCM08, available from 2020-05-16), and smoothing distances of 32, 16, 8, 4 km. We then relocate the full catalog using the 4km smoothing-length SSST corrections (Figure SSST_SEISMICITY?). The quality criteria for an event location and station-phase to be used for calculating $\bar{R}$ are: 68% error-ellipsoid principleaxis half-width ≤10.0 km, root mean square of residuals (rms) ≤0.2 sec, number of readings ≥10, azimuth gap ≤ 160°, P residual ≤ 1.0 sec, S residual ≤ 1.0 sec.

Methods S2. Absolute, coherency relocation

In a second relocation stage, we us a new procedure which greatly reduces aleatoric location error by combining information across absolute event locations based on waveform coherency between the events. This absolute, coherency relocation is based on the concept that if the waveforms at a station for two events are very similar (e.g. have high coherency) up to a given frequency, then the distance separating these events is small relative to the seismic wavelength at that frequency (*9*, *10*), perhaps less than about ¼ of the seismic wavelength at that frequency (*9*). A pair of similar events is a doublet and a set of similar events may be called a cluster, multiplet or family, these events all likely occur on a small patch of a fault with similar magnitude and source mechanism (*11*, *12*).

For detailed seismicity analysis, the precise hypocenter locations of events in multiplets can be assigned to a unique centroid point in space through some statistical combination of the initial absolute hypocenters. Alternatively, precise, differential times between like-phases (e.g. P and S) for doublet events can be measured using time- or frequency-domain, waveform correlation methods. Differential times from a sufficient number of stations for pairs of doublet events allows high-precision, relative location between the events, usually maintaining the initial centroid of the event positions (*10*, *13–18*).

Here we use waveform similarity directly to improve the precision of absolute locations without the need for differential time measurements. We assume that high coherency between waveforms for two doublet events implies events are nearly co-located, and also that all the information in the event locations, when corrected for true origin-time shifts, should be nearly identical in the absence of noise. Then, stacking procedures can be used to reduce the effective noise in this information and improve the location precision. We use the coherency between waveforms for pairs of events at one or more stations to combine through stacking an initial set of location probability density functions (PDF's). This stack directly improves the hypocenter locations, by effectively reducing noise in the arrival time data, velocity model and travel-times.

We measure waveform coherence as the maximum cross-correlation between two waveforms (e.g., *19*), calculated using the cross_chan_correlation function in the EQcorrscan Python package (*20*) which performs a normalized cross-correlation in the frequency-domain. Positive coherences, C, above a minimum cutoff value, C_{min}, (e.g. 0.45) to 1.0 are mapped linearly to 0.0 to 1.0 weights, W, for stacking location PDF's,

$$W = (C - C_{min}) / (1.0 - C_{min}). \quad \text{(S2)}$$

We use waveforms windows that include both P and S waves so that we maintain the S-P time interval, the P coda and part of the S coda, all of which better constrain waveform similarity for the purpose of absolute event locations. When the waveforms for multiple stations are available for a pair of events, we use the maximum coherency over stations as the inter-event coherency. This choice is justified since the coherency for real, noisy waveforms is much less likely to be over-estimated than under-estimated. The number of event pairs for which coherence is calculated can be reduced by only considering pairs with initial iner-hypocenter separation within a maximum cutoff distance (*19*).

The absolute, coherency relocation procedure requires a set of initial, absolute locations and corresponding PDF's for the spatial hypocenter locations. For each target event, the procedure forms a weighted stack of normalized PDF's over 3D space consisting of: the initial location PDF for the target event with a weight of 1, and, the location PDF weighted by W for each of the other events that have inter-event coherency with the target event greater than C_{min}. This PDF stack forms the probabilistic, coherence relocation for the target event and defines all the location information, such as origin time, uncertainties, and arrival-time residuals. This absolute, coherency relocation procedure can be implemented with a workflow using modules of the NonLinLoc package.

For an event that has coherency with all other events less than C_{min}, the stacked PDF location and location information will be identical to those for the initial location for the event. For an initial event that is poorly constrained with an extensive PDF, but which has high coherency with other, well constrained events, the stacked PDF location will shift to closely match those of the well constrained events. Since the absolute, coherency relocation can be performed with single station waveforms, it is efficient, and allows precise relocation of seismicity when the closest station is far from the seismicity, for sparse networks, and precise relocation of foreshocks and early aftershocks in a mainshock sequence or swarm before nearby temporary stations are installed.

The same weighting is used to combine first-motion readings between multiplet events. This produces a greater number of better constrained focal-mechanisms than with single event readings, though these mechanism are locally correlated across multiplet events.

For the Monte Cristo study, we measure coherency using vertical component waveforms at a permanent station NN.LHV.--.HHZ available through out the sequence and a temporary station near the M6.5 epicenter NN.MCA06.--.HHZ available from 2020-05-18. Waveforms are filtered from 2-10Hz in a window from 4 sec before the predicted P arrival to 4 sec after the predicted S arrival. The cross-correlation is applied over a sliding window of -2.0 to 2.0 sec, and the coherency weight is set linearly from 0.0 to 1.0 over coherency values from Cmin = 0.45 to 1.0. This procedure is applied to the full catalog, 2km SSST relocations (Figure SSST_SEISMICITY?) for all event pairs with a maximum hypocenter separation of 2.5 km. The final NLL-SSST-coherency relocations are shown in Figure SSST_COH_MAP.

Methods S3. FMAMP – Probabilistic focal-mechanism determination

FMAMP performs a probabilistic, global-search over focal mechanism strike, rake and dip using P-arrival, first-motion or amplitude data (*21*). FMAMP uses an efficient, oct-tree, importance-sampling search (*8*, *22*), outputs a set of mechanisms that follow the probability density function for the mechanism as constrained by the data, and evaluates solution quality based on wighted distribution (quasi-pdf) of P and T axes. FMAMP is based in part on the HASH focal mechanism method (*23*)

Supplementary Figures

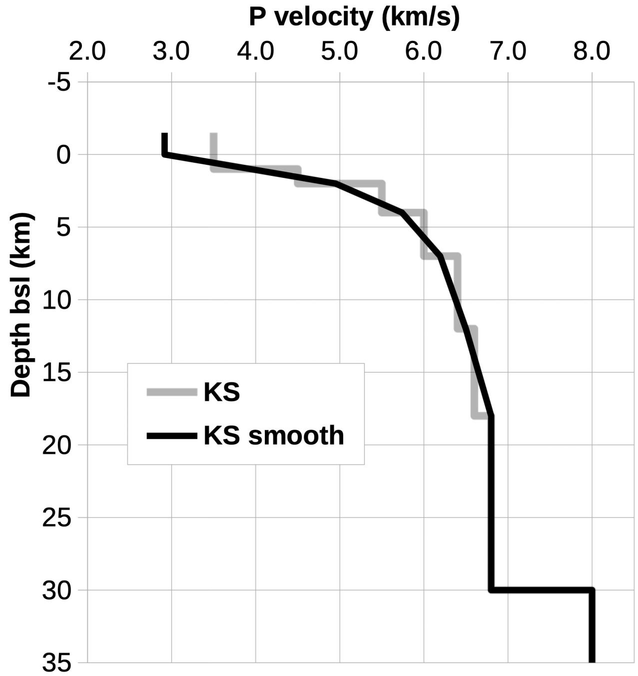

Fig. S1. Velocity models used for location. Original KS model P velocity profile (*24*) and slowness-smoothed version (KS smooth) used for initial NLL relocation.

a)

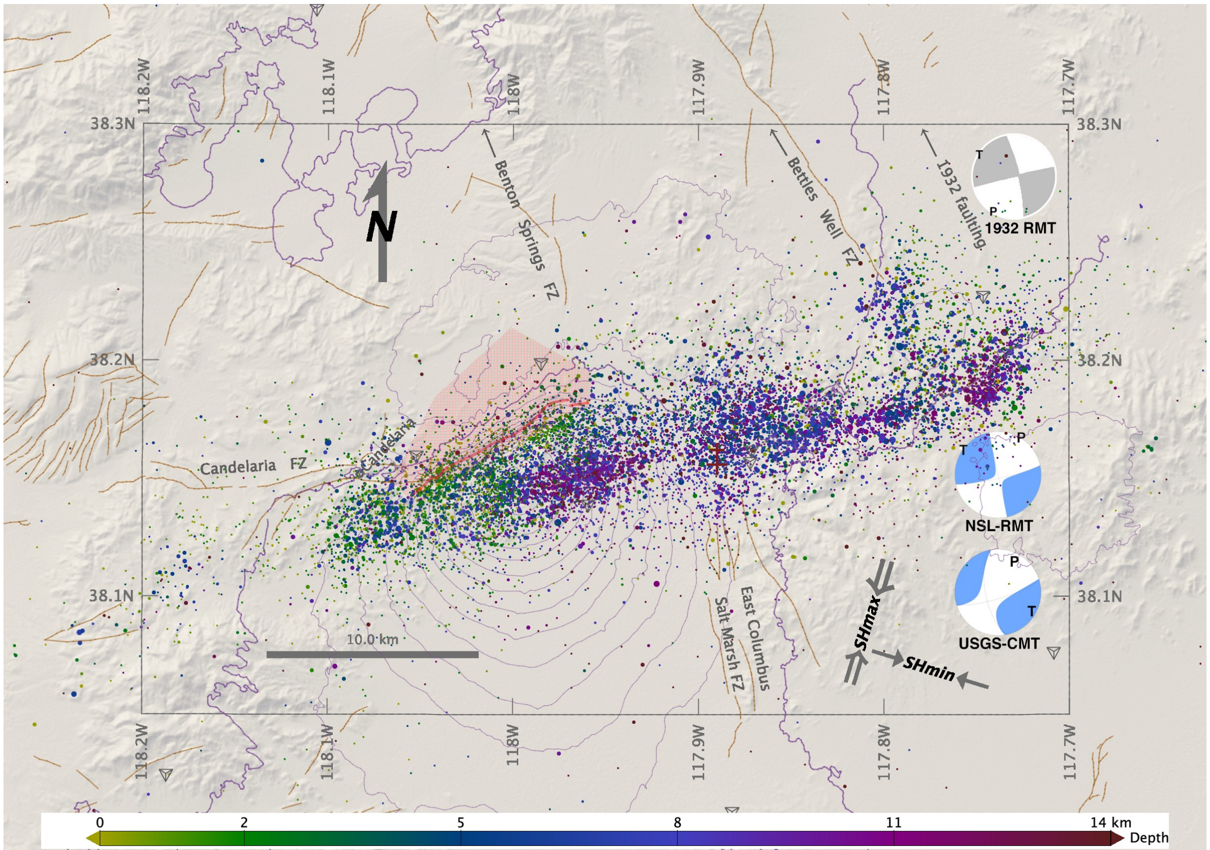

Fig. S2. Map view of Monte Cristo seismicity with different location procedures. Absolute locations for ~12,300 events 2020-01-01 to 2020-07-31 from a) USGS-NSL, b) NLL, b) NLL-SSST and d) NLL-SSST-coherence, no event quality filtering is applied. Event color corresponds to hypocenter depth and symbol size is proportional to magnitude. Re-picked Mw6.5 hypocenter and its proxy (mean hypocenter of 3 well constrained foreshocks) indicated by small and large, dark red, cross symbols, respectively. Blue focal mechanisms shows M6.5 mainshock USGS-CMT W-phase mechanisms and NSL-RMT regional moment tensor, gray mechanism shows the RMT for the, 1932 Mw 7.2 Cedar Mountain earthquake (*25*). Purple contours show Sentinel-1 vertical displacement (2 cm interval; heaviest contour indicates zero level; ~28 cm maximum subsidence; ~4 cm maximum uplift), thick light red line shows interpreted NE-SW afterslip (May 17 – May 23) with 2-3 cm of LOS displacement (*26*). Red shade shows area of dense mapped surface ruptures and fractures (*27*). SHmin and SHmax show directions of regional minimum and maximum compressive stress, respectively (from 3 closest data in *28*); the intermediate principal stress axis is vertical. Seismic stations shown as dark gray tetrahedrons. Brown lines show faults from the Quaternary fault and fold database for the United States. Background topography image from OpenTopgraphy.org.

b)

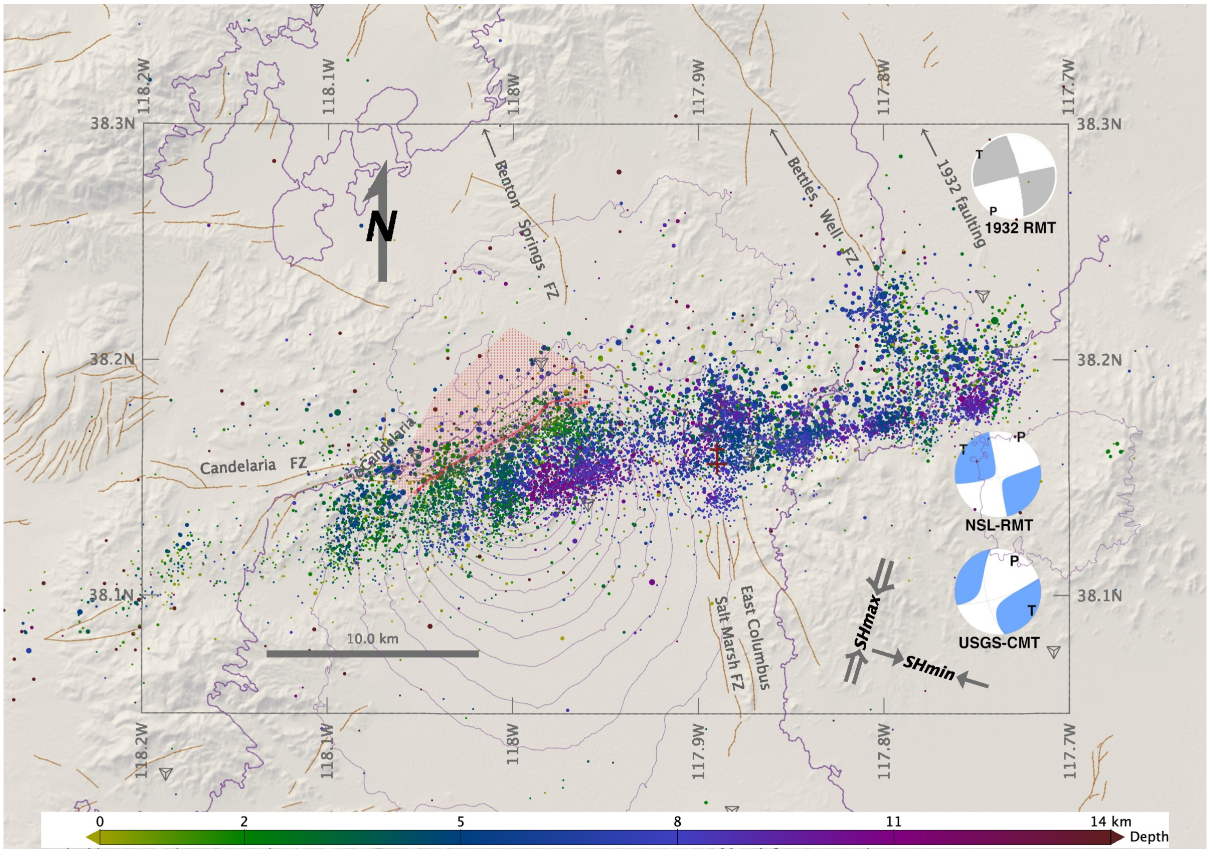

118.2W
118.1W
118W
117.9W
117.8W
117.7W
38.3N
38.2N
38.1N
N
Benton Springs FZ
Bettles Well FZ
1932 faulting
1932 RMT
Candelaria FZ
Candelaria
NSL-RMT
USGS-CMT
East Columbus
Salt Marsh FZ
SHmax
SHmin
10.0 km
0
2
5
8
11
14 km
Depth

c)

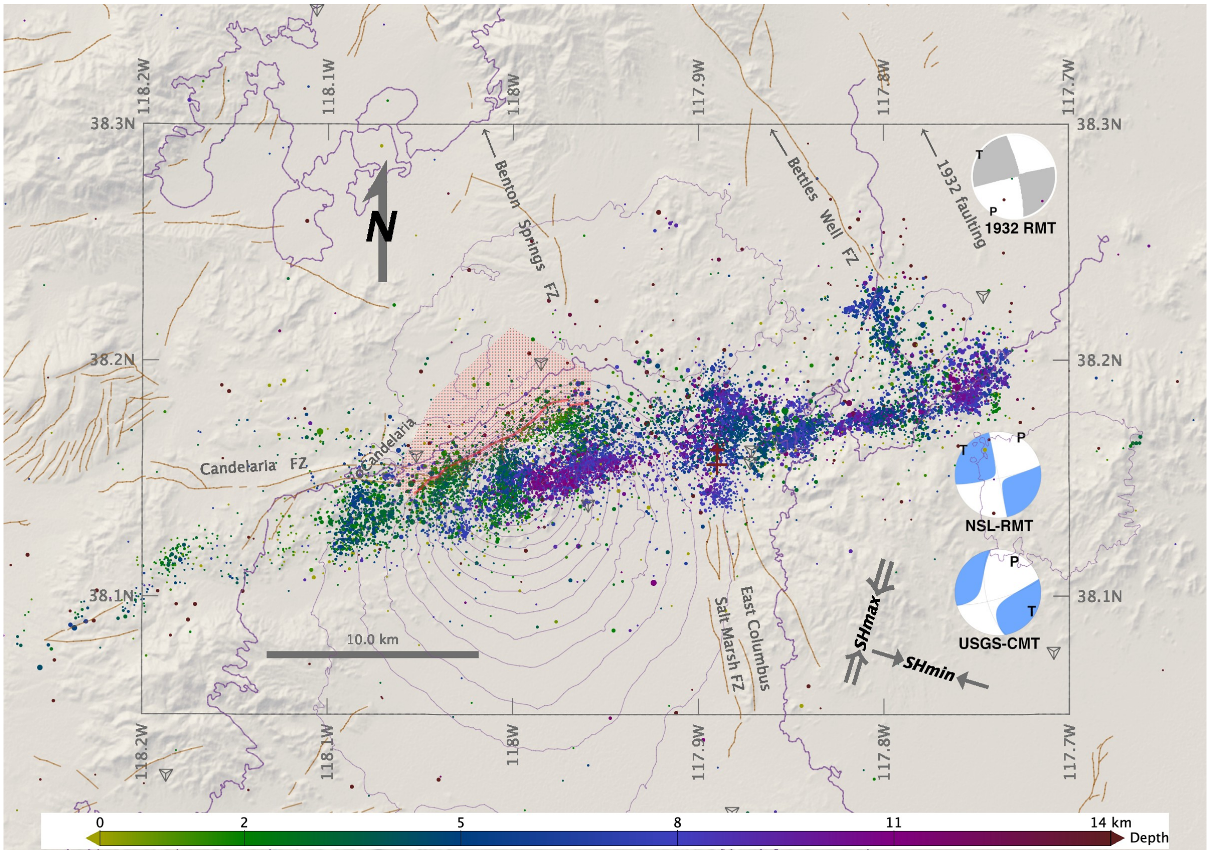

118.2W
118.1W
118W
117.9W
117.8W
117.7W
38.3N
38.2N
38.1N
N
Benton Springs FZ
Bettles Well FZ
1932 faulting
1932 RMT
T
P
Candelaria FZ
Candelaria
NSL-RMT
USGS-CMT
East Columbus
Salt Marsh FZ
10.0 km
SHmax
SHmin
0
2
5
8
11
14 km
Depth

d)

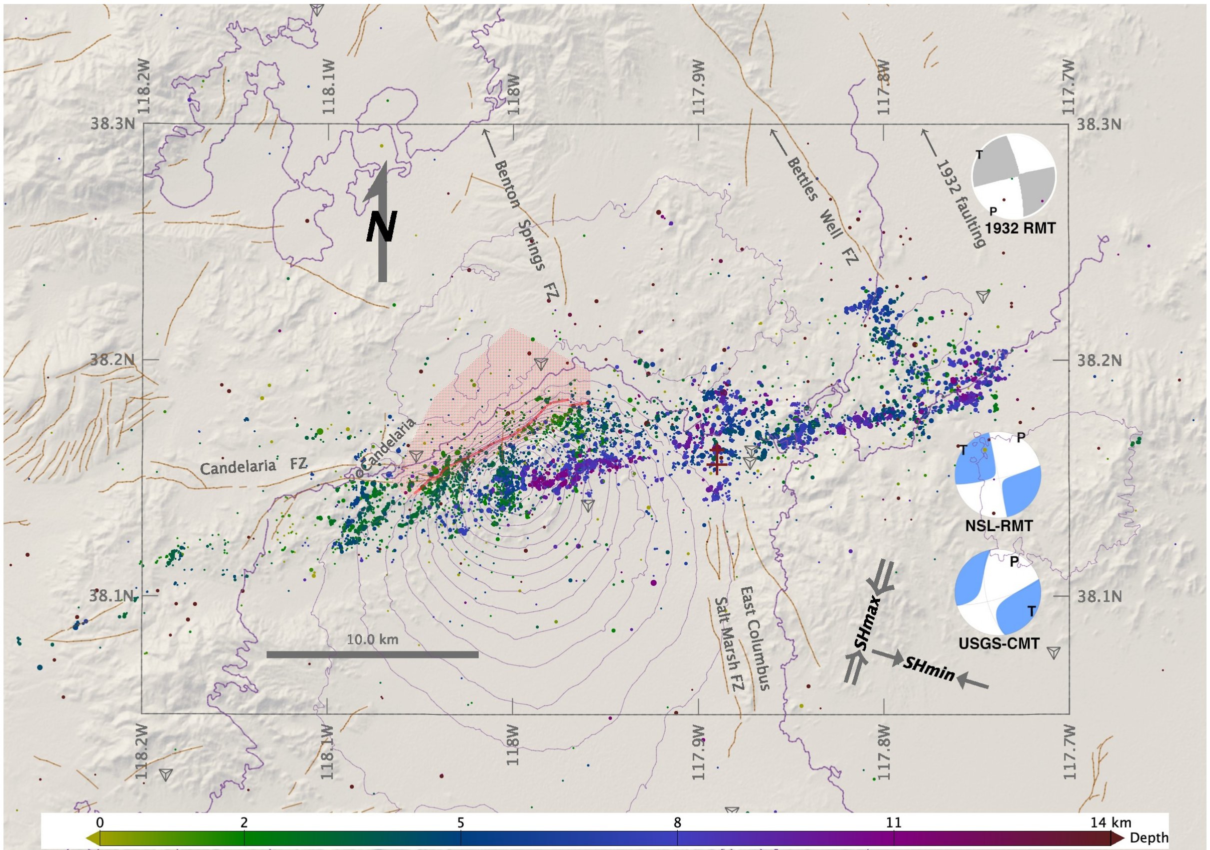
118.2W
118.1W
118W
117.9W
117.8W
117.7W
38.3N
38.2N
38.1N
N
Benton Springs FZ
Bettles Well FZ
1932 faulting
T
P
1932 RMT
Candelaria
Candelaria FZ
NSL-RMT
USGS-CMT
East Columbus
Salt Marsh FZ
SHmax
SHmin
10.0 km
0
2
5
8
11
14 km
Depth

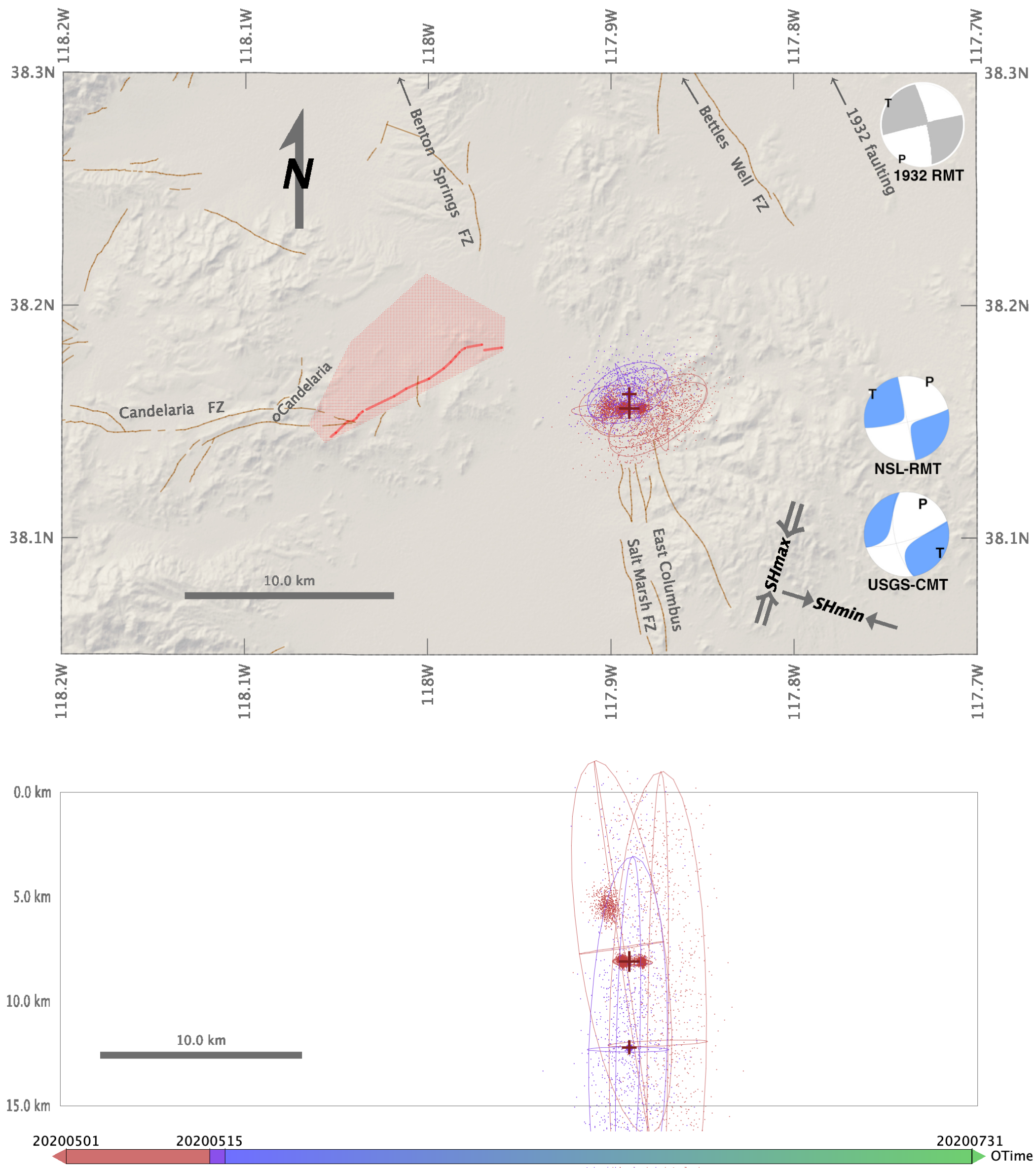

Fig. S3. Relocations of Monte Cristo mainshock and 5 foreshocks. Event color corresponds to origin time, mainshock hypocenter is large, violet dot. Clouds of small points show NLL location probability density functions (PDFs), ellipsoids show corresponding 68% confidence volumes. The PDF's and ellipsoids for the three multiplet foreshocks with well constrained coherence locations form a tight, double cluster above the mainshock hypocenter. Other map elements as in Fig. S2.

1 # References

1. K. B. Richards-Dinger, P. M. Shearer, Earthquake locations in southern California obtained using source-specific station terms. *J. Geophys. Res.* **105**, 10939–10960 (2000).

2. W. Tucker, E. Herrin, H. W. Freedman, Some statistical aspects of the estimation of seismic travel times. *Bulletin of the Seismological Society of America*. **58**, 1243–1260 (1968).

3. W. L. Ellsworth, Bear Valley, California, earthquake sequence of February-March 1972. *Bulletin of the Seismological Society of America*. **65**, 483–506 (1975).

4. C. Frohlich, An efficient method for joint hypocenter determination for large groups of earthquakes. *Computers & Geosciences*. **5**, 387–389 (1979).

5. A. Lomax, A Reanalysis of the Hypocentral Location and Related Observations for the Great 1906 California Earthquake. *Bulletin of the Seismological Society of America*. **95**, 861–877 (2005).

6. A. Lomax, Location of the Focus and Tectonics of the Focal Region of the California Earthquake of 18 April 1906. *Bulletin of the Seismological Society of America*. **98**, 846–860 (2008).

7. A. Lomax, J. Virieux, P. Volant, C. Berge-Thierry, in *Advances in Seismic Event Location*, C. H. Thurber, N. Rabinowitz, Eds. (Springer Netherlands, Dordrecht, 2000; http://link.springer.com/10.1007/978-94-015-9536-0_5), vol. 18 of *Modern Approaches in Geophysics*, pp. 101–134.

8. A. Lomax, A. Michelini, A. Curtis, in *Encyclopedia of Complexity and Systems Science*, R. A. Meyers, Ed. (Springer New York, New York, NY, 2014; http://link.springer.com/10.1007/978-3-642-27737-5_150-2), pp. 1–33.

9. R. J. Geller, C. S. Mueller, Four similar earthquakes in central California. *Geophys. Res. Lett.* **7**, 821–824 (1980).

10. G. Poupinet, W. L. Ellsworth, J. Frechet, Monitoring velocity variations in the crust using earthquake doublets: An application to the Calaveras Fault, California. *J. Geophys. Res.* **89**, 5719–5731 (1984).

11. M. Cattaneo, P. Augliera, D. Spallarossa, C. Eva, Reconstruction of seismogenetic structures by multiplet analysis: An example of Western Liguria, Italy. *Bulletin of the Seismological Society of America*. **87**, 971–986 (1997).

12. G. Ferretti, An Improved Method for the Recognition of Seismic Families: Application to the Garfagnana-Lunigiana Area, Italy. *Bulletin of the Seismological Society of America*. **95**, 1903–1915 (2005).

13. Y. Nakamura, A1 moonquakes: source distribution and mechanism. *Proc. Lunar and Planet. Sci. Conf. 9th*, 3589–3607 (1978).

14. G. Poupinet, F. Glangeaud, P. Cote, in *ICASSP '82. IEEE International Conference on Acoustics, Speech, and Signal Processing* (Institute of Electrical and Electronics Engineers, Paris, France, 1982; http://ieeexplore.ieee.org/document/1171796/), vol. 7, pp. 1516–1519.

15. A. Ito, High Resolution Relative Hypocenters of Similar Earthquakes by Cross-Spectral Analysis Method. *Journal of Physics of the Earth*. **33**, 279–294 (1985).

16. J.-L. Got, J. Fréchet, F. W. Klein, Deep fault plane geometry inferred from multiplet relative relocation beneath the south flank of Kilauea. *J. Geophys. Res.* **99**, 15375 (1994).

17. R. Nadeau, M. Antolik, P. A. Johnson, W. Foxall, T. V. McEvilly, Seismological studies at Parkfield III: microearthquake clusters in the study of fault-zone dynamics. *International Journal of Rock Mechanics and Mining Sciences & Geomechanics Abstracts*. **31**, 271 (1994).

18. F. Waldhauser, W. L. Ellsworth, A Double-Difference Earthquake Location Algorithm: Method and Application to the Northern Hayward Fault, California. *Bulletin of the Seismological Society of America*. **90**, 1353–1368 (2000).

19. R. C. Aster, J. Scott, Comprehensive characterization of waveform similarity in microearthquake data sets. *Bulletin of the Seismological Society of America*. **83**, 1307–1314 (1993).

20. C. J. Chamberlain, C. J. Hopp, C. M. Boese, E. Warren−Smith, D. Chambers, S. X. Chu, K. Michailos, J. Townend, EQcorrscan: Repeating and Near−Repeating Earthquake Detection and Analysis in Python. *Seismological Research Letters*. **89**, 173–181 (2018).

21. F. Bernardi, A. Lomax, A. Michelini, V. Lauciani, A. Piatanesi, S. Lorito, Appraising the Early-est earthquake monitoring system for tsunami alerting at the Italian Candidate Tsunami Service Provider. *Nat. Hazards Earth Syst. Sci.* **15**, 2019–2036 (2015).

22. A. Lomax, A. Curtis, in *Geophys. Res. Abstr.* (2001), vol. 3, p. 955.

23. J. L. Hardebeck, P. M. Shearer, A New Method for Determining First-Motion Focal Mechanisms. *Bulletin of the Seismological Society of America*. **92**, 2264–2276 (2002).

24. D. H. von Seggern, J. G. Anderson, I. M. Tibuleac, G. P. Biasi, Double-Difference Location and Ground-Truth Classification of the 2008 Mogul, Nevada, Very Shallow Earthquake Sequence. *Seismological Research Letters*. **86**, 146–157 (2015).

25. G. A. Ichinose, J. G. Anderson, K. D. Smith, Y. Zeng, Source Parameters of Eastern California and Western Nevada Earthquakes from Regional Moment Tensor Inversion. *Bulletin of the Seismological Society of America*. **93**, 61–84 (2003).

26. S. Valkaniotis, Interferograms for Monte Cristo EQ (2020), (available at https://doi.org/10.5281/zenodo.4273764).

27. A. J. Elliott, Dee, S., Koehler, R. D., Barnhart, W. D., Briggs, R., Collett, C., Dawson, T., DeLong, S., Gold, R. D., Haddon, E. K., Hartsorn, E., Hatem, A. E., Milliner, C., Pickering, A., Pierce, I., Seitz, G. G., Trexler, C., Wicks, C., Xu, X., & Zachariasen, J., Comparison of ground-based and space-based surface rupture mapping of the May 15, 2020 M6.5 Monte Cristo Range earthquake, Nevada. (2020), (available at https://www.scec.org/publication/10489).

28. J.-E. Lund Snee, M. D. Zoback, Multiscale variations of the crustal stress field throughout North America. *Nature Communications*. **11**, 1951 (2020).